Check for updates

Recyclable near-body temperature eutectic system with double positive temperature coefficient effect for personalised thermal regulation

Hongxu Guo, [a] Lichang Lu, [a] Kairen Zhao, [a] Huaiyu Yang, [b]
Helen Willcock, [a] Elisa Mele, [a] Xujin Bao, [a] Eileen Yu, [bc]
Han Zhang [d] and Yi Liu *[a]

Wearable temperature sensors are essential for medical and personal thermal management applications but often face challenges in achieving accuracy, flexibility and multifunctionality. To address these limitations, we developed a biodegradable polymer-based quaternary composite that leverages a binary eutectic fatty acid system and graphene nanoplatelets (GNPs) to deliver self-regulating heating and temperature sensing capabilities. The incorporation of polycaprolactone (PCL), lauric acid (LA) and myristic acid (MA) facilitates precise thermal control by enabling a tuneable phase transition range of 30 to 60 °C, while GNPs enhance electrical conductivity and thermal response. Notably, the material exhibits a distinct double positive temperature coefficient (PTC) effect, maintaining PTC behaviour up to 80 °C without transitioning to a negative temperature coefficient (NTC) effect. This double PTC behaviour enables precise thermal regulation, with self-regulating heating at ~36 °C under low-power operation (~100–250 mW), demonstrating stable power consumption and effective heat absorption through its phase change properties. The composite also supports operation under practical voltages, 5 V (standard power bank), making it well-suited for wearable systems. Additionally, the material demonstrates excellent recyclability through a simple dissolution and recasting process, retaining its stable thermal response even after recycling. These attributes make the composite highly suitable for electronic skins, smart thermal regulation and overcurrent protection fuses. The integration of PCL and fatty acids (FAs) enhances recyclability, promoting sustainable and long-term applications in personal thermal management systems.

New concepts

This work presents a novel biodegradable quaternary nanocomposite that integrates polycaprolactone (PCL), lauric acid (LA), myristic acid (MA) and graphene nanoplatelets (GNPs) to achieve a unique double positive temperature coefficient (PTC) effect near body temperature. By harnessing the eutectic behaviour of LA and MA, we finely tuned the phase transition range to 34–55 °C, enabling self-regulated thermal control precisely within physiologically relevant temperatures. Unlike conventional PTC composites that often suffer from a negative temperature coefficient (NTC) effect at higher temperatures or require rigid matrices and high voltages, our system maintains stable resistance up to 80 °C with no NTC behaviour and operates at low power (~4 V). This is enabled by the synergistic thermal expansion of the fatty acid eutectic and PCL matrix, which disrupts GNP conduction paths in a controlled manner. The result is a recyclable, low-voltage and flexible thermal material suitable for wearable electronics, including personal heating, safety fuses and electronic skin. This concept advances the field by combining eutectic phase engineering with smart conductivity modulation, offering a sustainable route toward next-generation adaptive thermal management materials.

1. Introduction

Maintaining a stable body temperature is critical for both medical monitoring[1,2] and sports applications,[3] particularly for individuals prone to overheating or at risk of temperature fluctuations.[4–8] Wearable temperature sensors and thermal regulation systems must effectively balance accuracy, flexibility, and multifunctionality, yet existing solutions often suffer from excessive bulk,[9,10] high energy consumption,[11–13] or poor recyclability. Addressing these challenges, the development of polymer-based nanocomposite systems with self-regulating thermal properties has emerged as a promising approach,[14–17] combining temperature sensing and heating functionalities in a single platform. In contrast to traditional metal-based devices, these nanocomposites enable real-time temperature monitoring alongside autonomous temperature regulation, effectively preventing overheating.

[a] Department of Materials, Loughborough University, Loughborough, LE11 3TU, UK.
E-mail: Y.Liu2@lboro.ac.uk

[b] Department of Chemical Engineering, Loughborough University, Loughborough,
LE11 3TU, UK

[c] School of Chemistry and Chemical Engineering, University of Southampton,
Southampton, SO17 1BJ, UK

[d] WMG, University of Warwick, Coventry, CV4 7AL, UK

However, despite their potential, polymer-based nanocomposites face several limitations, including high phase transition temperatures often exceeding 100 °C,[18,19] an ensuing negative temperature coefficient (NTC) effect and high energy consumption during manufacturing processes such as melt mixing, hot pressing and high-temperature curing, which require heating the polymer above its melting point, sustained mechanical energy for shear mixing and post-annealing treatments.[20–22] These limitations hinder their applicability in wearable systems designed to operate within the body temperature range, necessitating the development of more adaptable, energy-efficient, and recyclable materials.

Consequently, there is a critical demand for nanocomposites with tuneable thermal response ranges closer to body temperature, paired with energy-efficient production methods.[23–27] In response to these challenges, Hao *et al.* developed a hybrid positive temperature coefficient (PTC) material composed of silicon rubber, paraffin, graphite, and carbon nanotubes, achieving remarkable thermal stability across a wide temperature range (−20 °C to 120 °C) with a PTC intensity of 6.3, it does not exhibit a tuneable thermal response close to normal body temperature. Being exposed to 25 V for 50 seconds, the material maintained equilibrium temperatures for up to 7 minutes, achieving a surface temperature of approximately 30 °C, which could be a drawback for battery-powered wearable electronics, which often operate at much lower voltage (*e.g.*, 3–5 V).[28] To achieve superior thermal responsiveness, Luo *et al.* demonstrated a tuneable switching temperature with a high PTC intensity of 7.17, effectively suppressing the NTC effect near the glass transition temperature ($T_g \sim 109.5$ °C) of poly(methyl methacrylate) (PMMA) by varying filler concentration prior to melt mixing. However, despite these promising results, the inherent rigidity and processing constraints of PMMA limit its suitability for wearable applications, which demand materials with greater flexibility.[29] Addressing this need, Xue *et al.* introduced polyolefin elastomer (POE) as a secondary thermoplastic in HDPE/CB composites, significantly enhanced flexibility and achieved an impressive elongation at break of 980%.[30] This high flexibility underscores its potential for wearable electronics and soft robotics, yet the relatively high switching temperature remains a critical barrier to further application in these fields. In our previous study, we report a novel wearable temperature sensor based on a synergistic blend of lauric acid (LA), styrene–ethylene–butylene–styrene (SEBS), and graphene nanoplatelets (GNPs). This nanocomposite exhibits an exceptional PTC effect within the body temperature range (35–40 °C), achieving a four order of magnitude resistance change and a maximum temperature coefficient of resistance (TCR) of 471.4% °C^{-1}.[31] The integration of LA lowers the transition temperature while maintaining flexibility, addressing a key challenge in wearable PTC materials. Additionally, the sensor enables self-regulated Joule heating and passive cooling, offering precise temperature control with minimal energy consumption.

Notably, achieving efficient personalised heat dissipation without incurring excessive energy consumption remains a substantial challenge for widespread wearable applications.[32,33]

In general, cooling methods can be divided into two main categories: passive and active. Passive cooling, a mainstream approach, leverages the intrinsic properties of materials, particularly phase change materials (PCMs) with high melting enthalpy to absorb excess heat when temperatures surpass their transition point.[34–36] This approach is particularly appealing because it requires no external power supply, unlike active thermoelectric methods, making it especially suitable for applications where energy efficiency is paramount.[37–40] Liu *et al.* developed a novel, high-enthalpy (206.0 J g^{-1}), flexible nonwoven material by wet-spinning graphene and boron nitride, which retained 97.6% of its properties after 1000 thermal cycles. This high heat absorption capability enabled effective temperature regulation, maintaining stable thermal performance under prolonged use by keeping a body part (the face) at a temperature of 31.4 °C after 1410 s of solar illumination with intensity of 200 mW cm^{-2}.[41] Deng *et al.* used biomass cotton cloth and graphite nanoflakes fabricated a PCM reached up to a 293.7% higher thermal conductivity than pure paraffin wax with a large phase change enthalpy of 157.7 J g^{-1}. The utilisation of cotton cloth provides structural support, preventing leakage of the paraffin was during its phase transition, thus maintains its integrity and performance after 100 thermal cycles. During the heat dissipation test, the chip temperature can be cooled down to 40.3 °C from 70 °C.[42] Although many current studies have successfully prepared flexible PCMs with sufficient cooling property and stable shape, the procedures of such methods are often complex, requiring further development to transfer the technology into commercial large-scale production practice.

To address these challenges, a biodegradable binary eutectic fatty acid (FA) system with excellent shape stability and a flexible double-PTC effect film has been developed. This design exploiting the innovative use of a binary LA and myristic acid (MA) PCM matrix through their eutectic effect, the melting point of the binary PCM can be finely tuned. The addition of polycaprolactone (PCL) imparts the composite material with notable flexibility and enhanced thermal expansion. Furthermore, LA, MA and GNP were solution-mixed in varied ratios to optimise electrical and mechanical properties. Notably, the undesirable NTC effect following the PTC behaviour was eliminated and systematically investigated using DSC analysis. The microstructure and crystallisation behaviour, which are closely related to the double-PTC properties, were examined to reveal phase morphology and filler distribution across different compositions. Consequently, this novel FA eutectic system, embodied in the self-regulating PCL/LA/MA/GNP film, offers a promising balance between minimal power consumption and effective temperature regulation, especially suited for wearable devices designed to function in diverse environmental conditions.

2. Experimental

2.1 Materials

Polycaprolactone (PCL, Capa™ 6500, M_n = 50 000 g mol^{-1}) with a melting point of 58–60 °C and melt flow index (MFI) of 0.7 g min^{-1}

(2.16 kg, 160 °C) in pellets form was supplied from Ingevity UK Ltd. Lauric acid with the melting temperature region of 44–46 °C (W261408, M_w = 200.32 g mol^{-1}) and myristic acid with the melting region of 52–54 °C (W276413, M_w = 228.37 g mol^{-1}) were purchase from Sigma-Aldrich and used as received. Graphene nanoplatelets (GNP, Grade M, thickness of 6–8 nm and lateral dimension of 25 mm, surface area 120–150 m^2 g^{-1} according to XG Sciences) were purchased from Sigma-Aldrich. All the materials were dispersed in chloroform (Fisher Scientific UK, 67-66-3, 99.9+%, stabilised with amylene) to fabricate the nanocomposite film.

2.2 Double PTC film fabrication

PCL was mixed with lauric acid and myristic acid at various ratios and dissolved in chloroform, followed by the addition of 6.7 wt% GNP and dispersed in a glass vial using ultrasonic bath (Ultrawave – U300H, 35 W) at 50 °C for 1 hour. The nanocomposite mixture was then cast in a glass Petri dish (d = 80 mm) left to fully dry overnight at ambient temperature. After drying the nanocomposite mixture, the double PTC film was gently peeled off from the Petri dish with a material thickness of about 0.5 mm.

2.3 Characterisations

Scanning electron microscopy (SEM, JSM 7800F, JEOL) was employed to examine the morphology of the various nanocomposite samples. All film samples were imaged at cryo-fractured surfaces, prepared by immersing the samples in liquid nitrogen for 1 minute prior to fracturing. Each surface was sputtered with gold for 90 seconds before imaging, under an accelerating voltage of 5.0 kV.

Fourier transform infrared (FTIR) spectroscopy was performed using an Agilent Technologies Cary 630 FTIR spectrometer. Samples were placed on the cleaned sampling platform, ensuring intimate contact with the attenuated total reflectance (ATR) crystal, and spectra were acquired over a range of 4000–400 cm^{-1}. Following each measurement, the sampling platform and ATR crystal were thoroughly cleaned with soft cotton wipes to prevent cross contamination.

The heating performance of the smart thermal-regulating film was evaluated using an EA-3050B Elektro-Automatik AC power supply (0–300 V, 0.5–5 A), with applied voltages ranging from 0 and 24 V. Two K-type thermocouples (±0.01 °C), connected to a TC-08 temperature logger (Picotech), were used to monitor temperatures at two locations on the film surface to accurately track the sample temperature. To better visualise heat distribution, thermal infrared images were captured during both heating and passive cooling phases using a FLIR C3-X infrared camera. All the images were recorded with emissivity set to 0.97 with a measurement reading uncertainties of ±2%.

The pyro-resistive behaviour of the double PTC film was characterised by measuring the electrical resistance of fabricated samples as they were heated from ambient temperature to ~65 °C. This was performed in a Memmert UN55 oven at a controlled heating rate of 0.17 °C s^{-1}. PTC test samples, with average dimensions of 25 mm × 8 mm × 0.5 mm ($L \times W \times H$), were prepared by attaching aluminium foil strips as electrodes on each side, secured with silver paste (RS Pro) to minimise contact resistance and reduce strain interference from multimeter clips. After electrode attachment, samples were left to dry at room temperature (RT) for 10 minutes. Electrical resistance measurements were recorded using a Keysight 34465A digital multimeter, while temperature monitoring of both the sample and oven environment was conducted with a TC-08 temperature logger from Picotech.

The coefficient of thermal expansion (CTE) of the samples was measured using a TA Instruments Dynamic mechanical analysis (DMA) Q800, operating at a frequency of 1 Hz, with a temperature ramp of 5 °C min^{-1}, scanning from 0 to 65 °C under a controlled force of 0.01 N. Samples were prepared as rectangular bars with dimensions of 25 mm × 5 mm × 0.5 mm, three samples were tested from each composition to obtain an average value.

Different scanning calorimetry (DSC) was performed on the DSC Q200, TA instruments to investigate the latent heat and determine the crystallinity of the samples corresponding to the heating cycles. All the samples were chopped into pieces with an average mass between 6–10 mg. The heating temperature scan profile heat–cool–heat from 0 to 60 °C at a rate of 5 °C min^{-1} under nitrogen atmosphere (purging 50 ml min^{-1}). Reported values taken from TA universal analysis software. Each sample was tested at least three times, and the average values are reported.

All experiments involving human subjects (self-experimentation in the heating performance evaluation) were conducted in compliance with the principles of the Declaration of Helsinki. The participant provided informed consent prior to the experiments.

3. Results and discussion

3.1 Lauric acid and myristic acid binary eutectic system

Fig. 1(a) illustrates the theoretically predicted binary eutectic phase diagram for LA and MA, where points C and D represent the melting points of pure LA and MA, respectively. As the proportion of LA increases, the melting point of MA decreases; conversely, as the proportion of MA increases, the melting point of LA decreases, until the composition reaches the eutectic point (E). At this point, the composition and temperature represent the eutectic mass ratio and eutectic phase transition temperature. These eutectic mixtures, characterised by a single, sharp phase transition and defined enthalpy, are promising candidates for wearable temperature regulation and thermal energy storage applications.[43] Based on theoretical calculations (eqn (1)), the eutectic transition temperature for the LA/MA system is 34.34 °C, with a mass ratio of approximately 64.35% LA to 35.65% MA.

When mixing LA and MA, a binary mixture exhibiting an onset melting temperature higher than either pure component suggests a non-eutectic composition. However, increasing the content of one component gradually lowers the melting onset until the eutectic composition is achieved. The eutectic
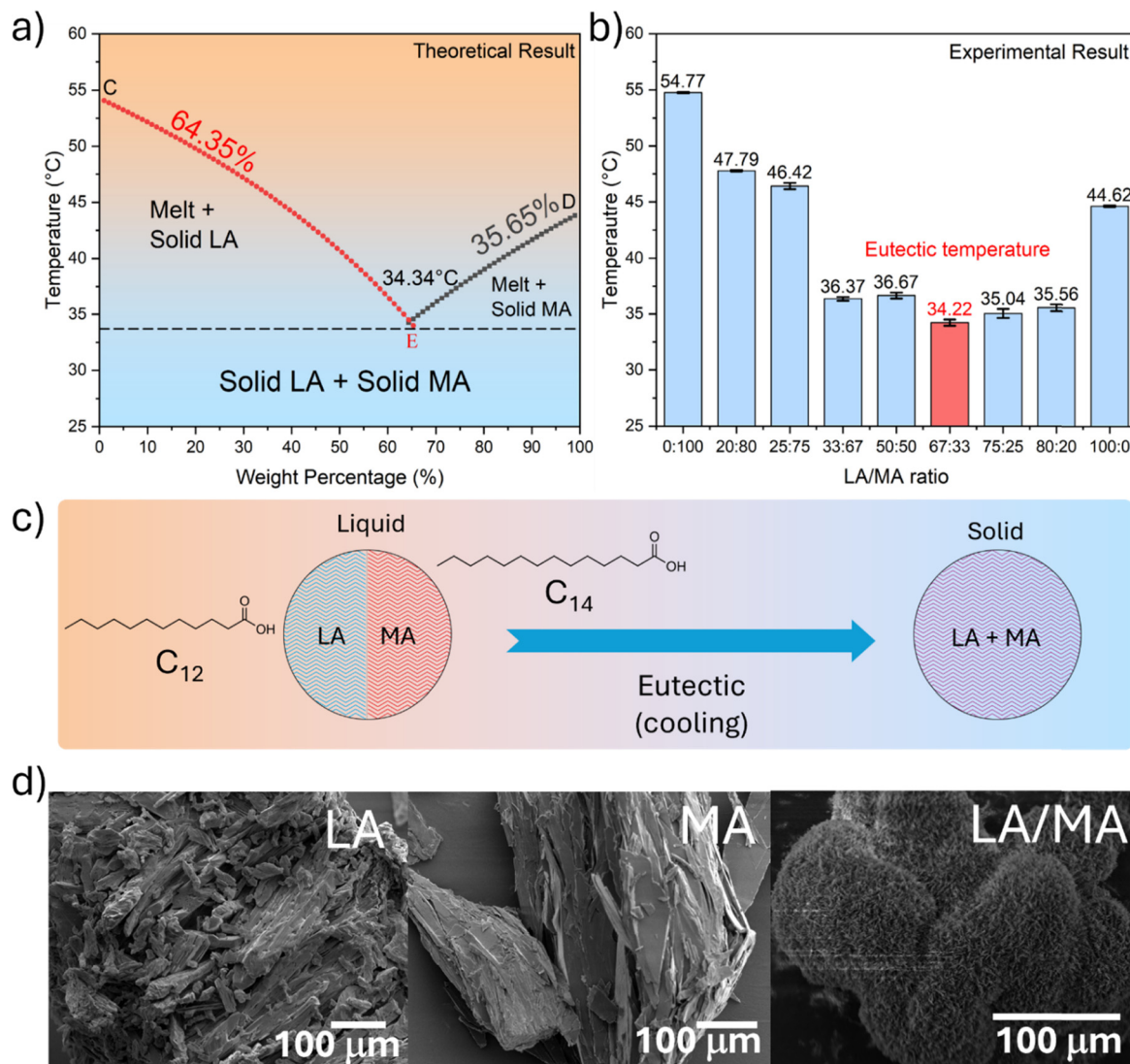
Fig. 1 (a) Theoretical calculation of the eutectic phase transition temperature for the LA/MA binary system. (b) Experimental DSC results showing the phase transition temperature of the different LA/MA binary composition mixture. (c) Illustration of the solid–liquid phase transition mechanism, highlighting microstructural transformations during the eutectic process. (d) SEM images depicting the morphologies of LA, MA, and the LA/MA binary eutectic mixture, demonstrating distinct microstructures before and after eutectic formation.

composition can be theoretically estimated using models such as Redlich–Kister,[44] Schroeder–Van Laar,[45] Schrader[46] and Schroder's equation.[47] Among these, the Schrader model is particularly advantageous due to its simplified assumptions and widespread applicability in engineering for predicting thermal parameters of eutectic systems.[48,49] Thus, the eutectic melting temperature can be calculating as follows:[43,48]

$$T_{\mathrm{m}} = \left(\frac{1}{T_{\mathrm{A}}} - \frac{R \ln X_{\mathrm{A}}}{\Delta H_{\mathrm{A}}} \right)^{-1} \qquad (1)$$

$$T_{\mathrm{m}} = \left(\frac{1}{T_{\mathrm{B}}} - \frac{R \ln X_{\mathrm{B}}}{\Delta H_{\mathrm{B}}} \right)^{-1} \qquad (2)$$

Here, T_{m} is the phase transition temperature of the eutectic mixture, T_{A} and T_{B} are the melting temperature of the pure material A and B, respectively. X_{A} and X_{B} are mole fractions of component A and B in the mixture ($X_{\mathrm{A}} + X_{\mathrm{B}} = 1$), respectively and ΔH_{A} and ΔH_{B} are the melting enthalpies of compound A and B and R is the gas constant (8.314 J K^{-1} mol^{-1}).

Eutectic PCMs are typically composed of materials that mix completely in their liquid state without undergoing a chemical reaction but remain immiscible upon solidification. This behavior allows eutectic systems to exhibit a sharp and reproducible melting point, which is advantageous for thermal energy storage and temperature regulating applications. The phase transition temperature of the eutectic mixture shifts to a lower melting point than that of each individual component due to the formation of a unique phase with total Gibbs free energy of the system minimised.[50] Such a eutectic effect was observed in the binary LA/MA eutectic mixtures while tailoring the temperature response range. There are three typical characteristics for

LA/MA eutectic: (i) there is no chemical reaction between the components mixed in the eutectic. (ii) The components are immiscible with each other in the solid phase, while completely miscible with each other in the liquid phase. (iii) The solid–liquid phase transition processes can only happen when the ambient temperature reaches the specific phase transition temperature of eutectic mixture.[19]

Fig. 1(b) showed the melting temperature of the binary systems of LA and MA, as determined by DSC analysis. The melting point of LA was decrease by the addition of MA; however, the melting point of MA remains largely unaffected by the addition of LA. At an LA/MA ratio of 20 : 80, the melting point decreases from 54.77 °C to 47.79 °C, and at a ratio of 80 : 20, the melting point decreases from 44.62 °C to 35.56 °C. This suggests that MA is more resistant to changes in melting point than LA. By DSC analysis, when the proportion of LA to MA in the mixture was about 64.35 : 35.65%, both components melted at the same time at a constant temperature, known as the eutectic phase transition temperature, which align well with the above calculated value. Table 1 shows the comparison of properties of the LA–MA eutectic mixture.

Such behaviour attributed to the molecular rearrangement in the solid phase at the eutectic mixture ratio upon re-crystallisation.[46] The eutectic phase transition temperature of LA and MA was 34.22 °C, aligning with the calculated theoretical value. The theoretical latent heat was determined as below:

$$H_m = T_m \sum_{i=1}^{n} \left[\frac{X_i H_i}{T_i} + X_i (C_{PLi} - C_{PSi}) \ln \frac{T_m}{T_i} \right], \quad (3)$$
$$(i = A, B)$$

where H_m is the latent heat of the binary eutectic system, J mol^{-1}, C_{PLi} is the specific heat at constant press of i-th substance at liquid state, and C_{PSi} is the specific heat at constant pressure of the i-th substance at solid state, J (g °C)$^{-1}$. In this study due to the molecular weight of the two components are sufficiently high, the error of the formula for latent can be negligible by the sensible heat. As for the long-chain organic compounds, the error is less than 4%.[51] Therefore, the formula can be simplified as:

$$H_m = T_m \sum_{i=1}^{n} \frac{X_i H_i}{T_i} \quad (4)$$

The calculated results have been compared with experiment data in this work and also work from,[43,45,46,52] which exhibited comparable results. Additionally, other group investigated eutectic mixtures of different FA combinations, ranging from capric acid (CA) to stearic acid (SA) (C_{10}–C_{18}), and the theoretical latent heat of binary eutectic mixtures (J g^{-1}) reported was within the range of 130.3 J g^{-1} to 177.2 J g^{-1}.

According to the material data provided by the supplier, the theoretical latent heat of the LA–MA binary eutectic system calculated in this work is 174.35 J g^{-1}, with the enthalpy of fusion, molecular weight and melting temperature of LA being 35.6 kJ mol^{-1},[53] 200.32 g mol^{-1} and 44.62 °C, respectively. The corresponding parameters for MA are 43.7 kJ mol^{-1},[53] 228.37 g mol^{-1} and 54.77 °C, respectively. The microstructural change illustration of the binary eutectic system are given in Fig. 1(c), when the temperature is above the melting point of both components it forms a single-phase solution over entire composition, the chains lose their ordered structure, where the molecules freely move and mix, become completely miscible and loses any phase boundaries present in the solid form. Upon cooling, when the composition is at the eutectic ratio (67.00:33.00), both components crystallise simultaneously as the temperature drops to 34.22 °C, forming an interlocking lamellar structure.[54] At compositions deviating from this ratio, one component crystallises first at a higher temperature, leading to non-uniform distribution of crystalline phases below 34.22 °C. Hence, such eutectic ratio is key to uniformity, while other ratios lead to sequential crystallisation and phase separation. The SEM images in Fig. 1(d) show the morphology of LA, MA, and the LA/MA eutectic system. The LA/MA eutectic mixture distributes uniformly in a porous structure, indicating good compatibility. This aligns well with previous research on capric acid (CA) and stearic acid (SA).[55] To further highlight the structural differences, the crystal morphology of LA and MA mixtures with different ratios, particularly those deviating from the eutectic composition (LA/MA 20 : 80 and 80 : 20) were examine as illustrated in Fig. S1.

The above results confirm that the melting temperature of the LA/MA binary mixture falls within the range of body temperature (34–55 °C), suggesting that the mixture exhibits eutectic behaviour at a specific composition. This characteristic highlights the potential of these eutectic mixtures for wearable devices, enabling efficient heat and cold regulation within a controllable active temperature range, thus offering promising applications for personalised thermal management.

3.2 Double PTC behaviour of PCL/eutectic mixture/GNP nanocomposites

A customised temperature-responsive range is in high demand for achieving personalised thermal management and temperature sensing across various age groups and applications, including athletes during sports,[56] newborn infants,[57,58] and elderly individuals with impaired thermoregulatory function.[6,59] Materials exhibiting the PTC effect[60] offer a promising approach, where electrical resistance increases with rising temperature due to disrupted conductive pathways during thermal expansion mismatch between the polymer matrix and conductive fillers.

Table 1 The theoretically calculated eutectic mass ratios, peak onset temperatures (T_m) and melting enthalpies (ΔH_m) and experimentally obtained corresponding values, with their absolute and relative differences of binary LA and MA eutectics

	LA–MA ratio (%)	Melting temperature T_m (°C)	Latent heat ΔH_m (J g^{-1})
Theoretical data	64.35 : 35.65	34.34	174.84
Experimental data	67.00 : 33.00	34.22 ± 0.27	184.00 ± 11.15
Absolute difference	2.65/2.65	0.12	10.56
Relative difference	3.96/8.03	0.35	5.74

The PTC intensity defined as the ratio of maximum to minimum resistivity within the transition region can be calculated as:[61]

$$\text{PTC intensity} = \log \frac{\rho}{\rho_0} \qquad (5)$$

where ρ represents the maximum resistivity and ρ_0 is the initial resistivity at ambient temperature. A double PTC effect, where resistance increases at two distinct temperature points, is particularly advantageous for applications requiring multi-stage thermal response, such as wearable healthcare systems or overcurrent protection circuits.[24,62]

To investigate the double PTC effect and switching behaviour in the nanocomposites, DSC analysis examined the melting transitions of various LA/MA compositions and assessed GNP incorporation effects on crystallisation behaviour. Fig. 2(a) shows DSC thermograms for seven different LA/MA weight ratios at a heating rate of 5 °C min⁻¹. The distinct melting points of LA and MA, combined with their eutectic phase behaviour, enable precise tuning of thermal transitions within the PCL matrix.

The 50 : 50 LA/MA blend exhibits a single eutectic melting peak near 35 °C. As MA content increases, this peak shifts to higher temperatures and separates into two distinct melting events, indicating phase segregation and enhanced thermal
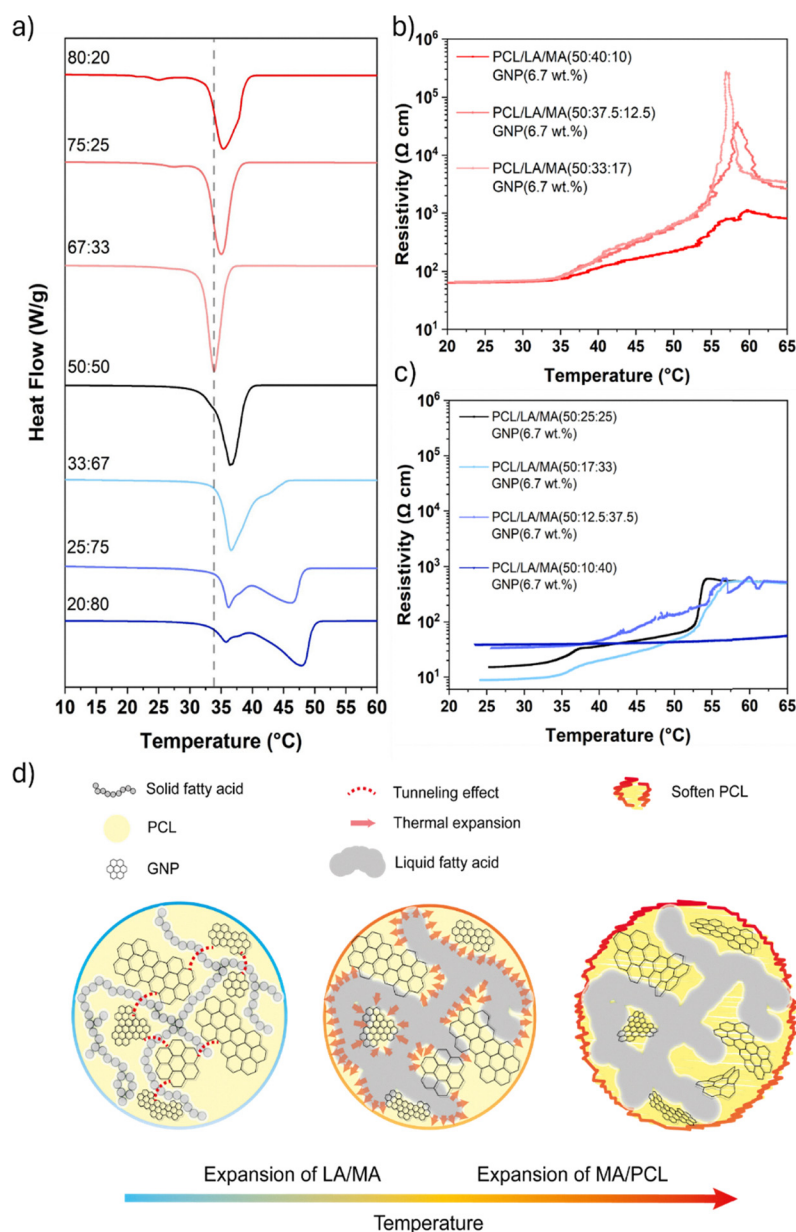

Fig. 2 (a) DSC results for seven different LA/MA eutectic systems. (b) and (c) The corresponding pyro-resistive effect of the seven different LA/MA eutectic systems, where the ratio between PCL and fatty acids was maintained at 50 : 50. (d) The mechanism of the double-PTC effect in the quaternary system.

stability. This improved thermal stability, especially at higher MA loadings, is critical for maintaining the structural integrity of the conductive GNP network during heating by reducing excessive viscosity changes during phase transitions.

The PCL, LA, MA and GNP weight ratios were systematically adjusted to achieve low electrical conductivity at RT while maximising PTC intensity. The differing melting points of LA and MA allow the design of dual thermal response ranges shifted around 45 and 55 °C. The resistivity-temperature curves (Fig. 2(b)) confirm that increasing MA content enhances PTC performance, with the 50 : 33 : 17 PCL/LA/MA formulation exhibiting the highest PTC intensity. However, this optimised formulation also shows a pronounced negative NTC effect at elevated temperatures, attributed to the significant viscosity drop in the molten LA/MA matrix, which promotes reformation of conductive pathways as GNPs come into closer contact.[16]

Interestingly, at specific PCL/LA/MA ratios (50 : 25 : 25 and 50 : 17 : 33), the double PTC phenomenon becomes more evident (Fig. 2(c)), with distinct resistive jumps at around 35 and 52 °C, corresponding to the melting transitions of the eutectic mixture and the PCL matrix. This dual-phase transition enables more sensitive and controlled temperature responses for personalised thermal management in wearable devices.

The underlying mechanism behind the observed dual PTC effect is illustrated in Fig. 2(d) and is governed by thermally induced structural changes in the composite. As the temperature increases and approaches the melting range of the LA/MA eutectic, the FA domains begin to soften and expand, introducing spatial mismatches among the conductive GNP fillers. Upon reaching the melting point of PCL, the combined expansion of both the PCL matrix and the MA component leads to a more pronounced disruption of the conductive network. GNPs become increasingly dispersed within the now fully molten FA matrix, breaking apart the percolated pathways required for electrical conduction. Although PCL has entered the NTC effect region beyond its melting point, in this case, the substantial volumetric expansion of MA dominates the structural dynamics. This results in a reduced local concentration of GNPs and suppresses the reformation of conductive pathways, thereby sustaining a high-resistance state even in the temperature range where NTC behaviour might otherwise emerge.

This proposed mechanism is further supported by DSC analysis (Fig. S2), which shows distinct endothermic transitions of LA (35.98 °C), MA (47.32 °C) and PCL (53.89 °C). These thermal events correspond directly to the sequential resistive jumps observed in the double-PTC behaviour, providing direct evidence for the mechanism proposed in Fig. 2(d).

Taken together, the sequential DSC transitions and the stable PTC response without NTC demonstrate that enhanced matrix expansion preserves inter-filler spacing and stabilises the percolated network at elevated temperature, thereby mechanistically suppressing conductive reconnection, this interpretation is further corroborated by CTE measurements discussed in Section 3.3 and is consistent with filler-matrix rearrangement observed in our previous work.[31]

Across various PCL/LA/MA compositions, RT resistivity decreases as the composition approaches the eutectic ratio of LA/MA. This behaviour is attributed to a reduction in the degree of crystallinity within the nanocomposite (see Table S1). The lower crystallinity promotes more uniform dispersion of GNPs within the amorphous regions, reducing agglomeration likelihood and leading to better electrical pathways and lower resistivity at RT.

The findings demonstrate that by carefully adjusting the eutectic composition, a customised temperature-responsive system can be designed where PTC intensity and switching temperatures are precisely controlled. This tunability is crucial for improving the reliability, sensitivity, and functionality of wearable systems, particularly in healthcare applications requiring continuous temperature monitoring and self-regulating behaviour.

3.2.1 NTC elimination. For polymer-based pyro-resistive materials, a major challenge has been mitigating the NTC effect while improving the reproducibility of the PTC effect.[27] This is crucial for extending the practical applications and usage cycles of these materials.[63] As shown in Fig. 3, the resistivity-temperature profiles of the various combination composite systems are compared.

In Fig. 3(a) (PCL/GNP), the resistivity remains stable up to around 60 °C, followed by a sharp increase that indicates a strong PTC effect. This corresponds to the melting of PCL, where the conductive network formed by GNPs is disrupted due to significant thermal expansion, especially during the melting of the crystalline phase.[64] Similarly, PCL/LA/GNP shows a comparable trend, but with an earlier PTC transition at approximately 37.5 °C, reflecting the lower melting point of LA. LA addition shifts the PTC onset to lower temperatures while maintaining a strong effect. However, the NTC effect occurred around 53 °C due to the decrease in viscosity of the polymer matrix. In contrast, the PCL/MA/GNP systems present a fluctuating resistivity curve with a transition above 55 °C while also demonstrating a lower PTC intensity, followed by an NTC effect. This is likely due to the high viscosity of MA, which restricted filler movement compared to LA. Finally, PCL/LA/MA/GNP showcases both a pronounced double PTC effect and the elimination of the NTC effect (see Video S1). The optimal composition was found as 60 : 10 : 30 ratio of PCL, LA and MA with 6.7 wt% GNP, which displays a two-step PTC behaviour and stabilises the overall PTC intensity at ~1.76 compared to the PCL/MA system. This well-balanced composition demonstrates reliable self-regulating capabilities, highlighting its potential for wearable thermal management applications.

The PTC and NTC behaviours of the polymer-based nanocomposite are schematically illustrated in Fig. 3(b). The PTC effect arises due to the isotropic thermal expansion of the polymer matrix (typically ~70–200 × 10^{-6} °C^{-1}), which increases the interparticle distance between the conductive fillers, leading to a sharp rise in resistance.[62] However, by further increase the temperature above the melting point (T_m), the polymer matrix undergoes a significant reduction in viscosity. This allows the nanofillers to rearrange and re-establish their conductive network,
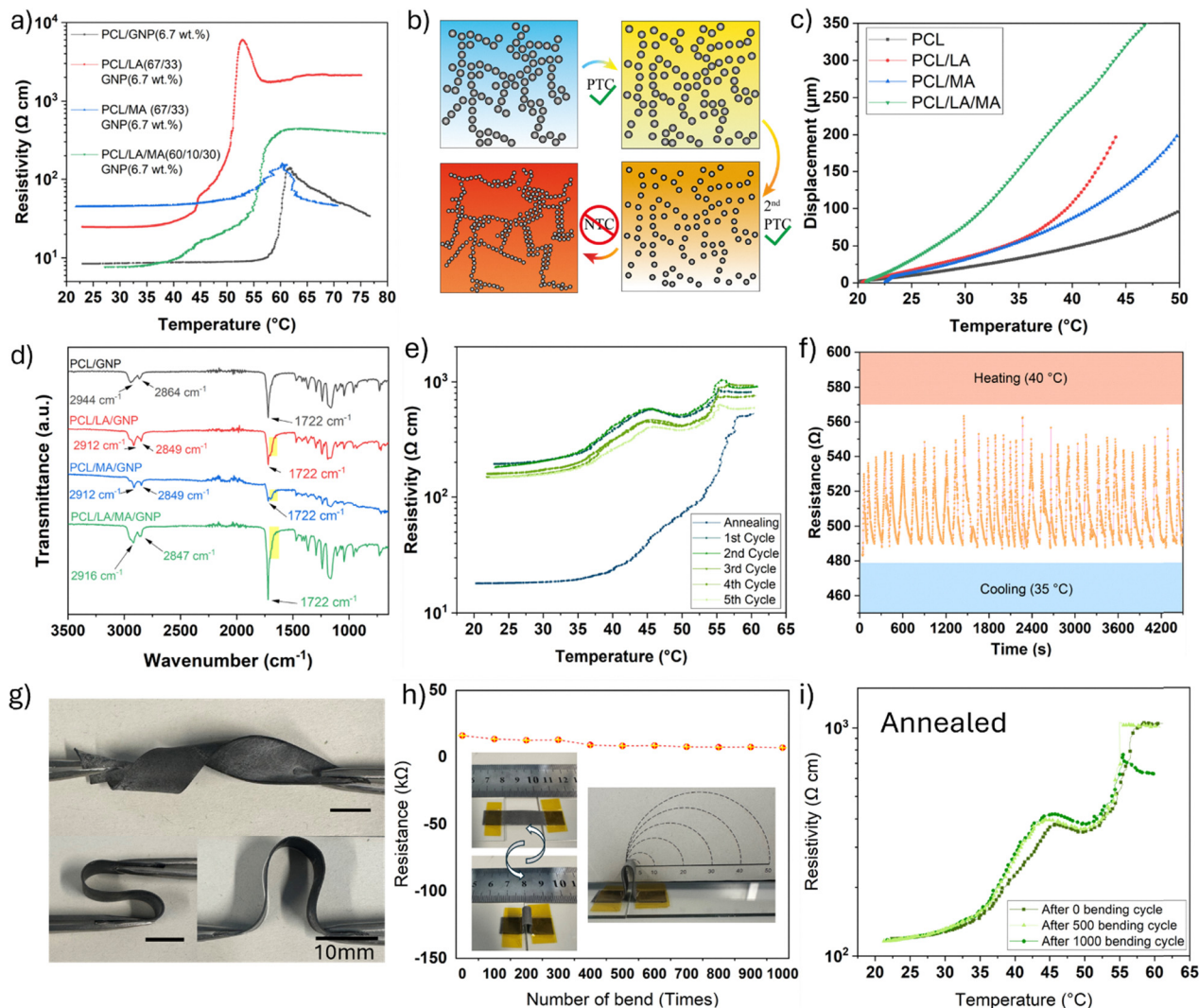
Fig. 3 (a) Pyro-resistive performance of PCL/GNP, PCL/LA/GNP, PCL/MA/GNP and PCL/LA/MA/GNP with their (b) FTIR scans, (c) schematic diagram of PTC and NTC formation due to thermal expansion of the housing matrix. (d) Coefficient of thermal expansion of different composite composites measured with DMA (e) repeatability of the thermal responsive behaviour of double-PTC film after heat annealing treatment. (f) Heat−cool cycles carried out using a heat gun. (g) Representative bent specimens illustrating deformation behaviour (scale bar: 10 mm). (h) Resistance stability during repeated bending up to 1000 cycles. Inset images show the bending setup with the sample mounted on two glass slides and deformed with a radius of 2.5 mm. The resistance remains nearly unchanged, confirming excellent mechanical robustness. (i) PTC effect characteristics before bending, and after 500 and 1000 bending cycles on separated samples. All curves exhibit consistent double-PTC behaviour with minimal deviation.

flowing more freely within the softened polymer matrix. This reorganisation forms a robust conductive network due to filler aggregation, causing a noticeable drop in resistance, a phenomenon referred to as the NTC effect. The occurrence of the NTC effect poses a challenge for the application of polymer-based PTC nanocomposites in electrical components, as it compromises the stability of their thermal and electrical performance. Fortunately, this challenge has been effectively addressed through the optimal composition of LA/MA, thanks to their large thermal expansion and a near body phase transition temperature, as shown in Fig. 3(c). DMA highlights the critical role of LA/MA in enhancing the composite's thermal expansion. From the calculated value, the incorporation of LA/MA increases the coefficient of thermal expansion from $166.7 \pm 55 \times 10^{-6}$ °C^{-1} (for the LA/MA-free

composite) to $520 \pm 84.9 \times 10^{-6}$ °C^{-1} (for the LA/MA-containing composite), indicating a substantial improvement in the material's ability to expand with temperature. This enhanced expansion alongside preserved viscosity facilitates greater separation between nanofillers, effectively disrupting the conductive network at the phase transition temperature. As a result, premature reconnection of conductive pathways is minimised, ensuring stable electrical resistivity above the transition point.

Their chemical structure was also characterised and compared by performing FTIR spectroscopy analysis. The FTIR spectra of prepared the individual PCL/GNP, FAs incorporated binary and the optimised double PTC composite as illustrated in Fig. 3(d). Their spectroscopy indicates no chemical reaction occurred during mixing, as the blend spectra retain the

characteristic absorption peaks of the individual components. The PCL component displays its distinctive triplet of characteristic peaks: the C=O stretching vibration at $\sim$1722 cm^{-1}, C–H stretching bands at $\sim$2849 cm^{-1} and $\sim$2916 cm^{-1}, and the C–O stretching vibration appearing as a plateau-like band in the 1150–1200 cm^{-1} region.[65] The FAs (LA and MA) exhibit their characteristic C=O stretching vibration at $\sim$1700 cm^{-1}, which is notably different from PCL's C=O peak position at $\sim$1722 cm^{-1}.[66] This peak shift is attributed to the different chemical environments of the carbonyl groups – PCL's ester carbonyl *versus* the carboxylic acid carbonyl in FAs. The distinct positions of these C=O stretching bands serve as a crucial indicator for confirming the presence of both components in the mixtures. Due to their similar molecular structures, differing only by two methylene groups, LA and MA show nearly identical FTIR spectra and cannot be distinguished solely through FTIR analysis (see Fig. S3b). However, their presence in the mixtures can be further confirmed through thermal analysis, as LA and MA possess distinct melting points. The absence of new peaks or peak shifts in the blended samples indicates no chemical interaction occurred between the components, suggesting a physical mixing process. Interestingly, such scans can also confirm the presents of the GNP containing in each sample, where the characteristic peaks of all organic components remain unchanged and it is evidenced by a characteristic declining baseline (increased slope) at wavenumbers below 1000 cm^{-1}, which is typical for graphene-based materials due to their inherent absorption properties. Also, the incorporation of GNP can be visually confirmed through a colour change of the samples to dark grey/black, while spectroscopically.

In Fig. 3(e), a reproducible thermal-responsive behaviour is achieved after annealing the nanocomposite in an oven. The material consistently exhibits double-PTC switching temperatures at 35 and 52 °C without showing any NTC effect. However, the RT resistivity increases from 18 Ω cm to 193 Ω cm, attributed to the reorganisation of the conductive network within the polymer matrix, likely caused by the relaxation of internal stresses during solvent evaporation in the fabrication process. The binary eutectic FA system (LA/MA) undergoes solid–liquid phase transitions near body temperature, contributing to the material's thermal responsiveness. After the first heat treatment, minor phase separation and re-crystallisation occur at RT, slightly reducing the uniformity of the conductive network formed by GNPs and leading to a small increase in resistivity. However, this initial reorganisation allows the GNPs to redistribute and form a more stable and efficient conductive network. Consequently, after this first rearrangement, subsequent heating and cooling cycles have minimal impact on the network's structure, resulting in stabilised resistivity. To simulate real-world scenarios, the thermal stability performance was also evaluated under repetitive transitions between hot and cold environments, as shown in Fig. 3(f). Specifically, the nanocomposite was subjected to alternating temperatures of 35 and 40 °C with a transition rate of 0.5 °C s^{-1} immediate transfer between pre-heated and ice-cooled plates.

The optimised nanocomposite exhibited stable double-PTC switching at $\sim$35 and $\sim$52 °C during heating, with cooling transitions at $\sim$31 and $\sim$48 °C. The resulting narrow hysteresis ($\sim$4 °C) confirms reproducible and reliable thermal response enabled by the eutectic LA/MA transitions and the flexible PCL matrix.

Furthermore, the PCL/LA/MA/GNP exhibits excellent flexibility and mechanical robustness, as demonstrated by their ability to sustain large bending and twisting deformation without fracture (Fig. 3(g)). To further evaluate durability, bending-fatigue tests were performed by repeatedly bending the PCL/LA/MA/GNP composites attached on two sliding glasses with radii of 2.5 mm for up to 1000 cycles. Electrical resistivity at RT ($\sim$20 °C) were recorded after every 100 cycles (Fig. 3(h)), and full PTC curves were recorded after every 500 cycles. The composites demonstrated excellent mechanical and electrical stability. PTC switching temperatures maintained within ±1 °C of their initial values and PTC intensity retention above 90%. No obvious NTC behaviour was observed up to 60 °C even after 1000 bending cycles (Fig. 3(i)). These results confirm reliable performance under physiologically relevant bending conditions representative of wearable use. To further validate the mechanical robustness of the composite under practical temperature variations, tensile testing was additionally conducted at both room temperature (23 °C) and elevated temperature (40 °C), shown in Fig. S4 and Table S2.

3.3 Morphology

From the results of the eutectic mixture PTC samples, it is evident that the drop in resistance can potentially be mitigated by slightly increasing the MA content in the eutectic system. This is because the higher phase transition temperature of MA stabilises the system's thermal behaviour by raising the overall eutectic temperature, thereby reducing the likelihood of a significant drop in matrix viscosity during phase transitions. Consequently, the conductive nanosheets are less likely to disperse excessively, preventing the resistance drop.

Additionally, the increased MA content enhances the structural integrity of the conductive network formed by GNPs. Fig. 4 presents cryo-fractured SEM images illustrating the morphological changes across single, binary, ternary, and quaternary systems. In the single-phase system, PCL and GNPs exhibit typical polymer sheet-like and wrinkled morphologies, respectively. In contrast, the microstructures of LA and MA show irregular crystalline formations, which can be attributed to the tight packing of their saturated FA chains. The absence of double bonds allows these FAs to form a stable crystalline structure, enhancing their solid-state stability.

As shown in Fig. 4(b), no signs of immiscibility are observed at the microscopic level within the binary systems, indicating good compatibility between each combination. The PCL/LA (67:33) and PCL/MA (67:33) systems demonstrate significant changes compared to their pure components. In both cases, the crystalline phase of the FAs appears reduced in size due to interactions with PCL, suggesting good miscibility between the components. No phase separation is visible, which further
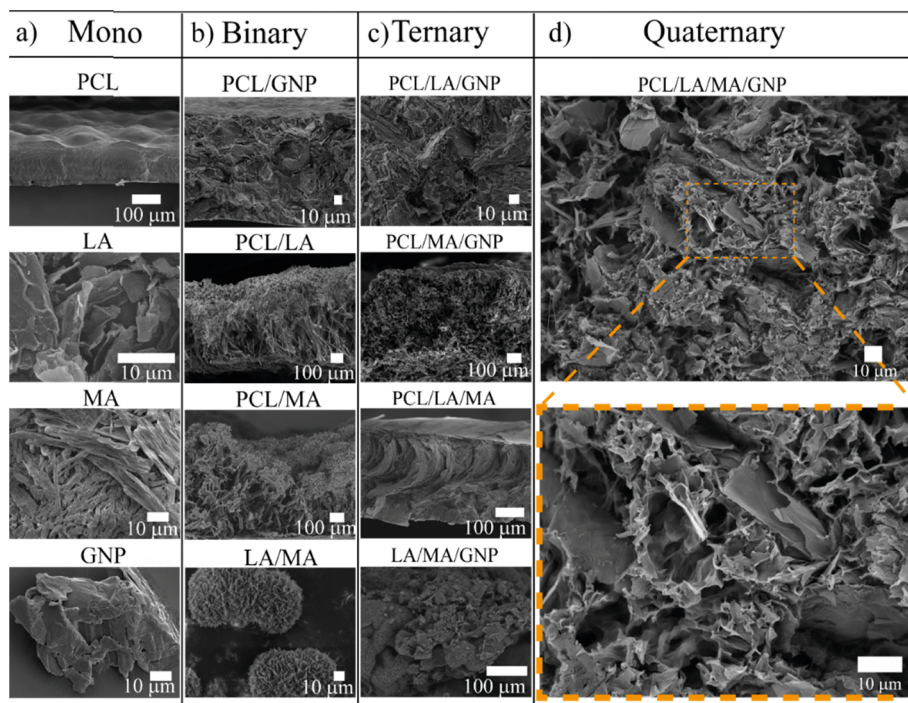
Fig. 4 RT SEM cross-section images of (a) single material PCL, LA, MA, GNP, (b) binary system, PCL/GNP, PCL/LA, PCL/MA, LA/MA, LA/GNP, MA/GNP, (c) ternary system PCL/LA/GNP, PCL/MA/GNP, PCL/LA/MA, LA/MA/GNP and (d) quaternary system PCL/LA/MA/GNP with zoomed in section.

supports compatibility between the polymer and FAs, potentially enhancing the mechanical properties and thermal regulation of these systems.

The LA/MA binary system shows an interwoven crystalline structure, likely due to eutectic formation between the two FAs, creating a more cohesive morphology than that of the individual LA and MA. Additionally, the introduction of GNPs into the binary systems of PCL/LA, PCL/MA and LA/MA results in noticeable morphological changes. In these ternary composites, GNPs are well-dispersed within the matrix and adhere to the crystalline structure of the FAs and polymer. This dispersion facilitates the formation of an interconnected conductive network, enhancing the electrical properties of the composite.

The PCL/LA/GNP, PCL/MA/GNP and LA/MA/GNP systems demonstrate that the inclusion of GNPs leads to improved initial electron tunnelling and percolation at RT, leaving potential for higher PTC intensity. The LA/MA/GNP system displays a more interconnected crystalline network, likely resulting in improved thermal and conductive properties due to synergistic interactions between the components.

Fig. 4(d) depicts the PCL/LA/MA/GNP composites, which exhibit the most intricate microstructures. The combination of LA and MA forms a co-continuous phase within the PCL matrix. This unique morphology enhances the phase change characteristics of the system, which are essential for low-temperature thermal regulation applications. The addition of GNPs in the PCL/LA/MA composite further improves the structural integrity of the conductive network, which is well-dispersed throughout the matrix, forming an interconnected network that surrounds thin barriers of matrix material. This co-continuous structure could potentially confine the liquid state of the FAs within the polymer domain, thus improving the reproducibility of the PTC effect, as illustrated in Fig. 3(f).

The interfacial energies of GNPs were calculated based on the surface energy of each component. The results indicate that the GNPs are likely to position themselves at the interface between MA and PCL (see Table S2), driven by the calculated interfacial surface energy at RT. Although surface energies can vary depending on the number of carbon atoms in the FAs, they typically range between 26 mJ m^{-2} and 39 mJ m^{-2}.[67,68] It is worth noting that the size of the GNPs can also influence their localisation, where larger GNPs (micro-sized) are more likely to be excluded from the crystalline regions during solidification and accumulate at the interphase, whereas smaller nano-sized GNPs may remain embedded within the crystalline matrix without significantly disrupting crystallisation.[69]

Consequently, a volume ratio of 30% MA was found to deliver the most pronounced double PTC effect and intensity while maintaining low RT resistivity. This balance ensures a smooth temperature response between the two self-regulating switching points, without triggering the NTC effect. The continuous thermal expansion of PCL around 60 °C disrupts the conductive network, minimising the NTC effect through the synergistic action of MA and PCL. Even when the temperature increased by 30 °C above the melting point of PCL, no NTC transition was observed. This demonstrates that PCL/LA/MA/GNP composites are highly suitable for self-regulating thermal applications, such as wearable temperature regulators and low temperature switching devices.

3.4 Self-regulating Joule heating

For heating element applications, a crucial parameter is the point at which the device begins to self-regulate, known as the PTC transition temperature. This is defined as the temperature at which half of the resistivity change is achieved on a logarithmic scale.[70] The dispersion and distribution of fillers significantly impact the self-regulating heating function.

Different filler arrangements influence the initial electrical properties and PTC intensity. Poor dispersion leads to agglomeration, which can obstruct electron pathways and reduce electrical conductivity. In contrast, well-dispersed but unevenly distributed fillers result in an increased filler-to-filler distance during heating, disrupting electron transport and producing a sharp resistance rise, thereby enhancing PTC intensity. When fillers exhibit both good dispersion and uniform distribution,

the larger interparticle distances hinder electron tunnelling, further affecting electrical conductivity.[18]

In general for composites with high filler content, the thermal expansion only slightly increases interparticle distances. This limited expansion prevents the complete destruction of conductive pathways, resulting in a weaker PTC effect. Conversely, composites with low filler content form fewer conductive pathways, leading to very high initial resistivity (ρ_0) and a weaker PTC effect overall.

As previously demonstrated, maintaining the GNP concentration at 6.7 wt% effectively reduces the initial resistivity and eliminates the NTC effect while preserving strong PTC intensity. Fig. 5(a) illustrates the heating performance of the quaternary PCL/LA/MA (60:10:30)/GNP (6.7 wt%) film under applied voltages ranging from 2 to 12 V. The data indicate a rapid temperature rise within a safe and controlled voltage
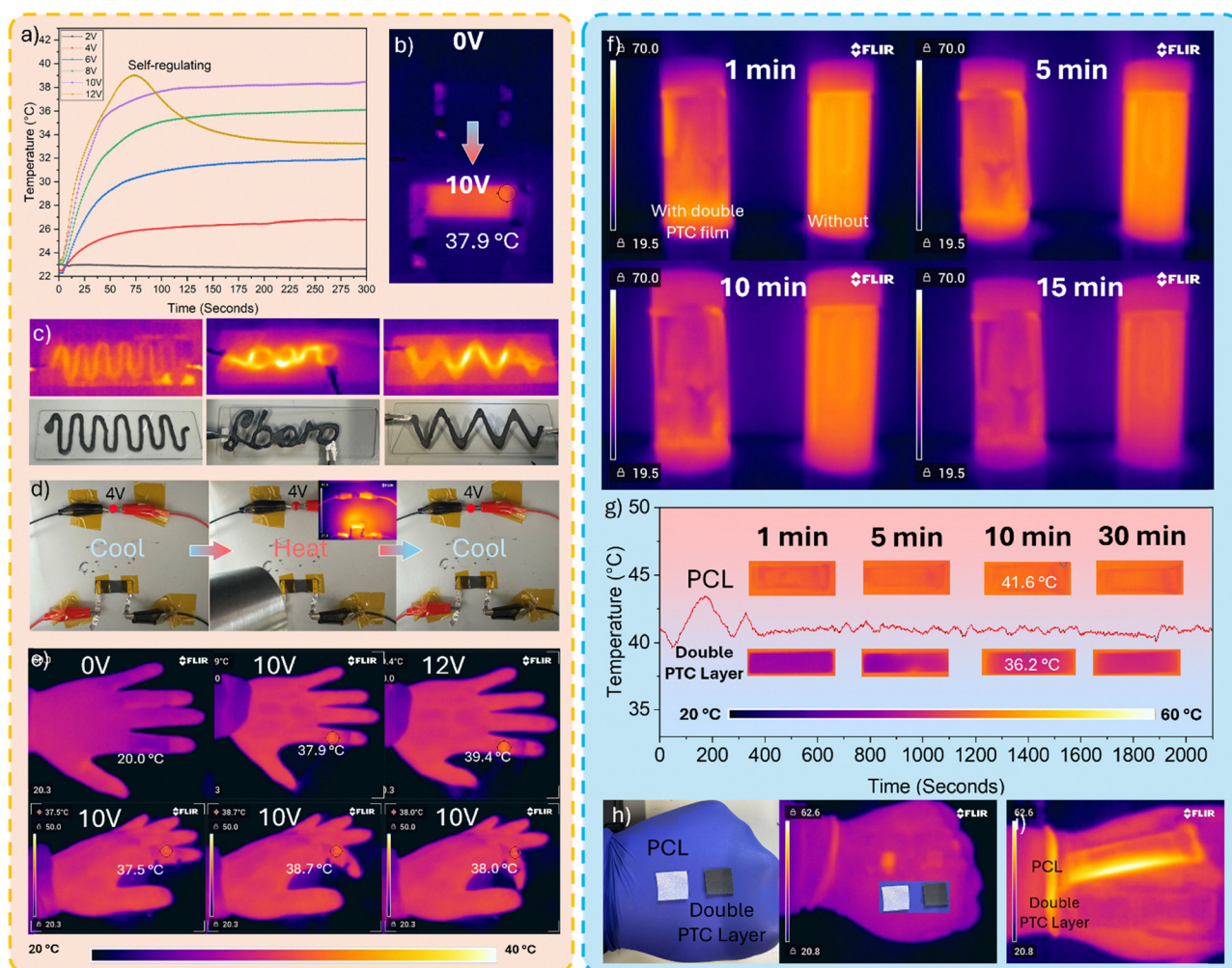

Fig. 5 (a) Self-regulating heating behaviour of the PCL/LA/MA/GNP composite under applied AC voltages ranging from 2–12 V. (b) IR images of the double-PTC nanocomposite demonstrating homogeneous heating performance. (c) Joule heating effect illustrated through various patterns created using the double-PTC ink. (d) Overheating protection circuit demonstration with excellent reproducibility. (e) Heating performance of the double-PTC film during bending tests conducted on an index finger at 45° and 90°. (f) Heat absorption test with the double-PTC film attached to a glass vial (left) filled with 60 °C water. (g) Heat stability test of the PCL and PCL/LA/MA/GNP films on a 40 °C hot plate. Heat resistance test of films attached to the back of the hand, exposed to 60 °C hot air. The pure PCL film is shown on the left (h) and top (i), while the PCL/LA/MA/GNP film is shown on the right (h) and bottom (i).

range. The heating layer stabilises over extended periods, and even when the voltage exceeds the set value, the nanocomposite exhibits self-regulating behaviour. Interestingly, a significant self-regulating behaviour was observed at 12 V, where the surface temperature initially rose to $\sim$39 °C within 75 s and then began to decrease due to a sharp increase in resistance. This rise in resistivity limited the current flow, effectively limiting further temperature increase by Joule heating.[25] Due to the eutectic behaviour of the PCL/LA/MA components, their melting points can be tailored to different ranges, as previously discussed. For comparison, films with PCL/LA/MA ratios of 50 : 33 : 17, 50 : 25 : 25, and 50 : 17 : 33 were analysed for self-regulating performance (see Fig. S5).

In Fig. 5(b), IR images demonstrate uniform heating capabilities, with the nanocomposite rapidly reaching epidermally suitable temperatures (up to 38 °C) under a 10 V input. Notably, the absence of the NTC effect ensures that resistivity does not decrease as temperature increases, thereby avoiding current spikes and potential overheating. The material's ability to maintain stable temperatures at different voltages highlights its potential for customisable heating garments that adapt to various environmental conditions and user preferences.

To further analyse the heating performance of the double-PTC composition, patterns with different shapes were fabricated using a 1 ml pipette tip, as illustrated in Fig. 5(c). The results demonstrate the material's excellent ability to achieve uniform and localised heating across diverse shapes. Furthermore, the double-PTC effect has potential applications in electrical circuits and batteries, where it could act as a failsafe mechanism, automatically limiting current flow to prevent excessive heating and potential damage. A demonstration of this overheating protection is shown in Fig. 5(d), where a circuit comprising an LED and the double-PTC film in series was tested. Under normal operating conditions at RT ($\sim$22 °C), the LED remained lit. When a heat gun was used to simulate sudden overheating ($\sim$52 °C), the circuit was effectively "cut off," causing the LED to extinguish as the resistance of the double-PTC film increased, limiting current flow and preventing potential fire hazards. Notably, the LED relit when the heat source was removed, showcasing the material's excellent reversible behaviour (see Video S2). As a flexible device, it is inevitable for the material to experience various deformations during daily use. To evaluate its heating performance under such conditions, the double-PTC film was tested for functionality during bending. As shown in Fig. 5(e), no significant impact on the heating performance was observed when the film was attached to an index finger and bent to a 45° and 90° angle, demonstrating excellent mechanical stability for wearable use. Beyond this simple test, systematic curvature experiments were also performed to further assess robustness. As shown in Fig. S6 and S7, with relative resistance changes remaining within ±0.1 across 10–50 mm between the original and recycled PCL/LA/MA/GNP films. These results confirm that mild deformation does not interfere with the self-regulating thermal response, underlining the suitability of the films for conformable applications. It should be noted, however, that extreme deformations beyond 45° and 90° are intrinsically limited in polymer-nanofiller networks, where excessive strain causes permanent pathway disruption. This behaviour is universal to such systems and not unique to the present composite, accordingly, our bending-fatigue and on-skin tests at radii down to 2.5 mm provide a realistic and practically relevant benchmark for wearable operation.

On the other hand, the FA component enables the film to absorb heat, further enhancing its effectiveness as a personal thermal management device. Benefiting from the tenable phase transition temperature of the binary eutectic system, the double-PTC film demonstrates efficient cooling performance. For instance, as shown in Fig. 5(f), a glass vial filled with hot water (60 °C) cools more rapidly when the double-PTC film is applied (left). Additionally, when comparing the bare PCL film and the double-PTC film on a hot plate set to 40 °C (simulating a fever temperature), the double-PTC film maintains a temperature of 36.2 °C for over 30 minutes, indicating superior cooling efficiency (Fig. 5(g)). Furthermore, two samples were tested by placing them on the back of the hand and exposing them to hot air at 60 °C, as shown in Fig. 5(h). The double-PTC film exhibited a surface temperature that was 8–10 °C lower than that of the PCL film.

In addition, the effective thermal resistance ($R_{\text{th,eff}}$) and heat flux (q) were estimated from the measured temperature differences and applied heating/cooling power (see SI for details). In the vial cooling test (Fig. 5(f)), the composite film exhibited a heat flux (q) of approximately 0.12 W cm^{-2}. In the hot-plate test (Fig. 5(g)), the film reduced the steady-state surface temperature from 40 to 36.2 °C, corresponding to $q = 0.38$ W cm^{-2}. For the hand exposure test (Fig. 5(h)), the double-PTC film maintained a surface roughly 8–10 °C cooler than pure PCL, with $q = 0.04$ W cm^{-2} under convective hot-air conditions. While radiative contributions were not explicitly included, these approximate values, together with consistent double-PTC switching, demonstrated the film's potential for versatility thermal management in wearable scenarios.

3.5 Recyclability

To achieve true sustainability in functional nanocomposites, it is crucial to assess their recyclability, minimising environmental impact. As illustrated in Fig. 6(a), the fabricated PCL/LA/MA/GNP films were successfully recycled through a simple process by cutting the films into small pieces, dissolved them in chloroform for 30 minutes, and then re-casting the solution in a glass Petri dish to form a new film. The pyro-resistive behaviour and self-regulating heating properties of the recycled film were systematically compared with the original film (Fig. 6(b)–(d)). Interestingly, the recycled film exhibited a slightly enhanced PTC effect, as shown in Fig. 6(b), indicating an improved resistivity transition at elevated temperatures and no significant of NTC effect was observed more than 80 °C, fulfil the need for portable electronic overheating protections. Additionally, the Joule heating performance under different applied voltages (Fig. 6(c)) demonstrated that the recycled film maintained stable and self-regulating heating behaviour, effectively limiting the maximum temperature to a
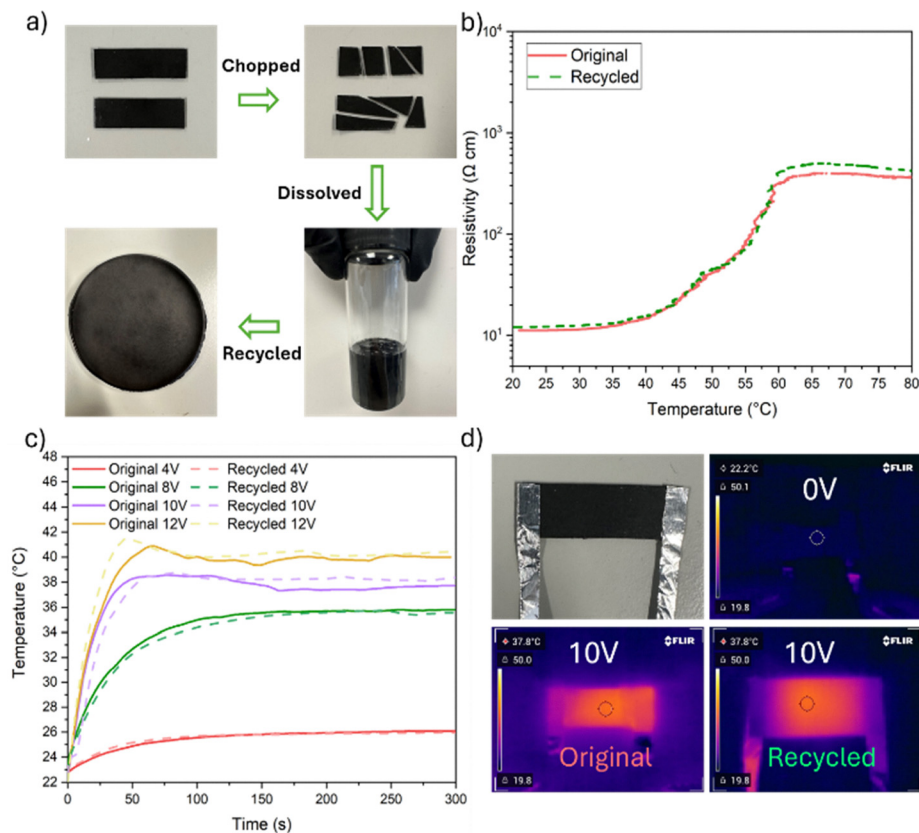
Fig. 6 (a) Recycling process of PCL/LA/MA/GNP nanocomposite film. (b) Comparison of PTC effects between original and recycled films. (c) Joule heating performance of the original and recycled films under different applied voltages (4, 8, 10 and 12 V). (d) Infrared (IR) thermal images comparing heating performance at 10 V.

safe range (∼42 °C) even at 24 V, see Fig. S8. Infrared thermography (Fig. 6(d)) further confirmed that the heating uniformity of the recycled film remained comparable to the original.

To further clarify, the present demonstration represents a proof of concept of recyclability, a single recycling cycle has shown sufficient retention of critical performance metrics, including resistivity, PTC intensity, switching temperature and Self-regulate Joule-heating behaviour. While multiple cycles would provide further confirmation of robustness, the solution-casting approach inherently ensures full redispersion of fillers and matrix, with negligible solvent residues due to chloroform volatility.

Overall, these results highlight the remarkable recyclability of the PCL/LA/MA/GNP nanocomposite films, extending their end-of-life usability while maintaining key functional properties. This reinforces their potential for sustainable and long-term use in wearable thermal management systems.

4. Conclusions

This study demonstrates the development and optimisation of a quaternary PCL/LA/MA/GNP nanocomposite for self-regulating thermal applications, with a particular focus on wearable temperature regulation. By carefully analysing the interfacial

energies of the components and their influence on filler dispersion, it was found that GNPs preferentially localise at the interface between the eutectic phase and PCL, primarily driven by their respective surface energies. However, it is important to note that the physical size of GNPs also plays a critical role in determining their final distribution. As temperature increases, the complex interaction between the expansion of MA and PCL influences the distribution of conductive GNPs, effectively preventing the formation of an NTC effect. The optimised composition (30% MA) exhibited a stable double PTC effect with precise self-regulating switching points at ∼45 and ∼55 °C, ensuring smooth temperature control with low power consumption. Self-regulating Joule heating tests confirmed effective temperature stabilisation across low nominal voltages (12 and 24 V), making this composite suitable for wearable regulators, low temperature switching devices, and electronic overheating protection. Additionally, the nanocomposite demonstrated excellent recyclability. Recycled films fabricated through a simple dissolution and recasting process, retained key functional properties, including a slightly enhanced PTC effect, stable Joule heating behaviour and uniform thermal distribution. This underscores the material's potential for sustainable, long-term applications in wearable thermal management systems, balancing high performance with environmental responsibility.

Author contributions

Hongxu Guo: data curation, investigation, formal analysis methodology, conceptualisation, writing – original draft, review & editing. Lichang Lu: methodology, formal analysis, writing – review & editing. Kairen Zhao: methodology, formal analysis, writing – review & editing. Huaiyu Yang: writing – review & editing. Helen Willcock: writing – review & editing. Elisa Mele: writing – review & editing. Xujin Bao: writing – review & editing. Eileen Yu: writing – review & editing. Han Zhang: funding acquisition, conceptualisation, writing – review & editing. Yi Liu: funding acquisition, methodology, resources, supervision, formal analysis, project administration, conceptualisation, writing – review & editing.

Conflicts of interest

There are no conflicts to declare.

Data availability

All data supporting the finding of this study, including experimental data, analytical results (*e.g.* DSC, SEM, FTIR and electrical measurements) and processing parameters are included in the main article and its supplementary information (SI). Supplementary information is available. See DOI: https://doi.org/10.1039/d5mh01491c.

Additional raw data are available from the corresponding author upon reasonable request.

Acknowledgements

References

1 Y. Geng, G. Chen, R. Cao, H. Dai, Z. Hu, S. Yu, L. Wang, L. Zhu, H. Xiang and M. Zhu, *Nano-Micro Lett.*, 2024, **16**, 1–14.

2 K. Yuan, Q. Chen, M. Qin, S. Gao, Q. Wang, S. Gao, F. Xiong, Y. Lv and R. Zou, *Adv. Funct. Mater.*, 2024, **34**, 1–29.

3 Y. Zhang, J. Fu, Y. Ding, A. A. Babar, X. Song, F. Chen, X. Yu and Z. Zheng, *Adv. Mater.*, 2023, **2311633**, 1–12.

4 Y. Liu, H. Zhang, H. Porwal, J. J. C. Busfield, T. Peijs and E. Bilotti, *Polym. Int.*, 2019, **68**, 299–305.

5 Y. Wang, T. D. S. Thorn, Y. Liu, S. G. Advani, D. G. Papageorgiou, E. Bilotti and H. Zhang, *Composites, Part A*, 2025, **192**, 108779.

6 N. Ndlovu and B. N. Chungag, *Aging Heal. Res.*, 2024, **4**, 100189.

7 A. L. Moore and L. Shi, *Mater. Today*, 2014, **17**, 163–174.

8 Y. Liu, H. Zhang, H. Porwal, W. Tu, J. Evans, M. Newton, J. J. C. Busfield, T. Peijs and E. Bilotti, *Adv. Funct. Mater.*, 2017, **27**, 1–9.

9 T. C. Ernst and S. Garimella, *Appl. Therm. Eng.*, 2013, **60**, 316–324.

10 Z. Hou, X. Liu, M. Tian, X. Zhang, L. Qu, T. Fan and J. Miao, *J. Mater. Chem. A*, 2023, **11**, 17336–17372.

11 B. Yang, X. Zhang, J. Ji, M. Jiang and Y. Zhao, *Appl. Therm. Eng.*, 2024, **257**, 124416.

12 Z. Li, M. Zhang, T. Yuan, Q. Wang, P. Hu and Y. Xu, *Energy Build.*, 2023, **278**, 112600.

13 S. Apoorva, N. T. Nguyen and K. R. Sreejith, *Lab Chip*, 2024, 1833–1866.

14 Y. Liu, T. van Vliet, Y. Tao, J. J. C. Busfield, T. Peijs, E. Bilotti and H. Zhang, *Compos. Sci. Technol.*, 2020, **190**, 108032.

15 Y. Liu, H. Zhang, H. Porwal, W. Tu, K. Wan, J. Evans, M. Newton, J. J. C. Busfield, T. Peijs and E. Bilotti, *J. Mater. Chem. C*, 2018, **6**, 2760–2768.

16 Y. Liu, E. Asare, H. Porwal, E. Barbieri, S. Goutianos, J. Evans, M. Newton, J. J. C. Busfield, T. Peijs, H. Zhang and E. Bilotti, *Composites, Part A*, 2020, **139**, 106074.

17 L. Lu, H. Guo, Y. Wang, K. X. Liu, I. Martin-Fabiani, T. Peijs, E. Bilotti, H. Zhang and Y. Liu, *Composites, Part A*, 2025, 109167.

18 Y. Liu, H. Zhang and E. Bilotti, *Polym. Nanocompos. Mater.*, 2021, 247–266.

19 K. Liu, Z. Xu, J. Mei, J. Han, F. Zheng, H. Wang, Y. Huang, Q. Wu, G. Qin, J. Jiang and Q. Li, *J. Mater. Chem. C*, 2023, **11**, 4966–4992.

20 S. R. Nicholson, N. A. Rorrer, A. C. Carpenter and G. T. Beckham, *Joule*, 2021, **5**, 673–686.

21 M. Dulal, S. Afroj, J. Ahn, Y. Cho, C. Carr, I. D. Kim and N. Karim, *ACS Nano*, 2022, **16**, 19755–19788.

22 Y. Li, T. D. S. Thorn, Y. Wang, A. Soul, Y. Liu, D. Papageorgiou, T. Peijs and H. Zhang, *Compos. Sci. Technol.*, 2025, **270**, 111294.

23 Y. Wang, B. Das, T. D. S. Thorn, S. Huo, J. Evans, M. Newton, Y. Liu, S. G. Advani, D. G. Papageorgiou, E. Bilotti and H. Zhang, *Appl. Mater. Today*, 2024, **39**, 102292.

24 X. Yao, Y. Wang, T. D. S. Thorn, S. Huo, D. G. Papageorgiou, Y. Liu, E. Bilotti and H. Zhang, *ACS Appl. Mater. Interfaces*, 2023, **15**, 56265–56274.

25 Y. Wang, X. Yao, T. D. S. Thorn, S. Huo, H. Porwal, M. Newton, Y. Liu, D. Papageorgiou, E. Bilotti and H. Zhang, *Compos. Sci. Technol.*, 2023, **239**, 110062.

26 G. Balzamo, X. Zhang, W. A. Bosbach and E. Mele, *Polymer*, 2020, **186**, 122087.

27 Y. Wang, B. Das, T. D. S. Thorn, Y. Liu, D. G. Papageorgiou, E. Bilotti and H. Zhang, *Compos. Sci. Technol.*, 2025, 111203.

28 J. M. Hao, Y. F. Yang, Y. T. Shen, R. Zhou, W. Zhang, H. Chen and W. L. Cheng, *Chem. Eng. J.*, 2024, **493**, 152427.

29 X. Luo and D. W. Schubert, *Mater. Today Commun.*, 2022, **30**, 103078.

30 F. Xue, K. Li, L. Cai and E. Ding, *Adv. Polym. Technol.*, 2021, 1124981.

31 H. Guo, L. Lu, F. L. Hatton, L. Xu, E. Yu, T. Peijs, E. Bilotti, H. Zhang and Y. Liu, *Adv. Funct. Mater.*, 2025, **2417961**, 1–13.

32 L. Li, W.-D. Liu, Q. Liu and Z.-G. Chen, *Adv. Funct. Mater.*, 2022, **32**(22), 2200548.

33 J. Li, Y. Zhou, C. Jiang, D. Lei and X. Yu, *J. Mater. Chem. C*, 2024, **12**, 12179–12206.

34 X. Zhang, K. Sun, H. Liu, J. Chen, X. Yan, Y. Kou and Q. Shi, *Nano Energy*, 2024, **121**, 109256.

35 Y. Shi, C. Wang, Y. Yin, Y. Li, Y. Xing and J. Song, *Adv. Funct. Mater.*, 2019, **29**, 1–8.

36 L. Lu, H. He, H. Guo, I. Martin-Fabiani, E. Bilotti, H. Zhang, A. Fly and Y. Liu, *Adv. Sci.*, 2025, **08314**, 1–14.

37 S. Ren, M. Han and J. Fang, *Polymers*, 2022, **14**(24), 5522.

38 H. Xu, B. Cao, L. Gao, F. Wang, G. Jin and Z. Liu, *Build. Environ.*, 2024, **250**, 111169.

39 L. Lu, H. Guo, I. Martin-Fabiani, Y. Zhou, H. Willcock, G. T. Vladisavljević, J. J. C. Busfield, E. Bilotti, T. Peijs, H. Zhang and Y. Liu, *EcoMat*, 2025, **7**(4), e70004.

40 L. Xiong, C. Chen, K. Tian, X. Zhang, M. Wen, C. Guo, M. Cheng, Q. Li, Q. Fu and H. Deng, *Adv. Mater.*, 2025, **2504150**, 1–10.

41 H. Liu, F. Zhou, X. Shi, K. Sun, Y. Kou, P. Das, Y. Li, X. Zhang, S. Mateti, Y. Chen, Z. S. Wu and Q. Shi, *Nano-Micro Lett.*, 2023, **15**, 1–12.

42 M. Deng, Y. Xu, K. Gao, C. Zhao, N. Sheng, C. Zhu and Z. Rao, *Appl. Therm. Eng.*, 2024, **245**, 122908.

43 H. Ke, *Appl. Therm. Eng.*, 2017, **113**, 1319–1331.

44 R. Wang, J. Chen, Z. Song and Z. Qi, *Ind. Eng. Chem. Res.*, 2023, **62**, 5382–5393.

45 P. Zhao, Q. Yue, H. He, B. Gao, Y. Wang and Q. Li, *Appl. Energy*, 2014, **115**, 483–490.

46 L. Shilei, Z. Neng and F. Guohui, *Energy Build.*, 2006, **38**, 708–711.

47 Z. Fan, Y. Zhao, X. Liu, Y. Shi and D. Jiang, *ACS Omega*, 2022, **7**, 16097–16108.

48 B. Liu, S. Wang, W. Jia, J. Xie, Z. Lu, H. Ying and Y. Sun, *Buildings*, 2023, **13**(12), 3043.

49 H. Nazir, M. Batool, M. Ali and A. M. Kannan, *Appl. Therm. Eng.*, 2018, **142**, 466–475.

50 M. Sun, T. Liu, H. Sha, M. Li, T. Liu, X. Wang, G. Chen, J. Wang and D. Jiang, *J. Energy Storage*, 2023, **68**, 107713.

51 Y. Yanping, T. Wenquan, C. Xiaoling and B. Li, *J. Chem. Eng. Data*, 2011, **56**, 2889–2891.

52 Q. He, H. Fei, J. Zhou, W. Du, Y. Pan and X. Liang, *Mater. Today Commun.*, 2022, **32**, 104058.

53 F. H. B. Sosa, N. D. D. Carareto, G. J. Maximo, A. J. D. A. Meirelles and M. C. Costa, *J. Chem. Eng. Data*, 2019, **64**, 5017–5027.

54 A. K. Pandey, B. Kalidasan, Z. Said, Y. K. Mishra and J.-Y. Hwang, *Mater. Today Sustain.*, 2024, **27**, 100934.

55 S. Liu, X. Zhang, X. Zhu and S. Xin, *ACS Omega*, 2021, **6**, 17988–17998.

56 T. W. Cheung, T. Liu, M. Y. Yao, Y. Tao, H. Lin and L. Li, *Text. Res. J.*, 2022, **92**, 1682–1693.

57 Y. Luo, M. R. Abidian, J. H. Ahn, D. Akinwande, A. M. Andrews, M. Antonietti and Z. Bao, *et al.*, *ACS Nano*, 2022, **17**(6), 5211–5295.

58 L. Xie, X. Wang, X. Zou, Z. Bai, S. Liang, C. Wei, S. Zha, M. Zheng, Y. Zhou, O. Yue and X. Liu, *Small*, 2023, **19**, 1–15.

59 M. Jose, A. Bronckaers, R. S. N. Kumar, D. Reenaers, T. Vandenryt, R. Thoelen and W. Deferme, *Sci. Rep.*, 2022, **12**, 1–14.

60 G. Zhu, F. Wang, L. Chen, C. Wang, Y. Xu, J. Chen, X. Chang and Y. Zhu, *Compos. Sci. Technol.*, 2022, **217**, 109133.

61 J. Meyer, *Polym. Eng. Sci.*, 1973, **13**, 462–468.

62 E. Barbieri, E. Bilotti, Y. Liu and C. Grimaldi, *Phys. Rev. Mater.*, 2024, **8**, 1–9.

63 Y. Wang, X. Yao, T. D. S. Thorn, S. Huo, H. Porwal, M. Newton, Y. Liu, D. Papageorgiou, E. Bilotti and H. Zhang, *Compos. Sci. Technol.*, 2023, **239**, 110062.

64 W. Di, G. Zhang, J. Xu, Y. Peng, X. Wang and Z. Xie, *J. Polym. Sci., Part B: Polym. Phys.*, 2003, **41**, 3094–3101.

65 T. Elzein, M. Nasser-Eddine, C. Delaite, S. Bistac and P. Dumas, *J. Colloid Interface Sci.*, 2004, **273**, 381–387.

66 X. Dong, Q. Li, D. Sun, X. Chen and X. Yu, *Food Anal. Methods*, 2015, **8**, 857–863.

67 T. Techapirom, S. Phankosol, S. Puttala, T. Chum-In and K. Krisnangkura, *J. Phys. Conf. Ser.*, 2018, **1144**(1), 012177.

68 M. Saito and A. Yabe, *Text. Res. J.*, 1984, **54**, 18–22.

69 Z. Lin, W. Tian, Y. Su, V. K. Yadav and H. Yang, *Particuology*, 2023, **79**, 27–34.

70 R. Strümpler, *J. Appl. Phys.*, 1996, **80**, 6091–6096.